

Difference imaging from single measurements in diffuse optical tomography: a deep learning approach

Shuying Li^{1b},^a Menghao Zhang,^b Minghao Xue^{1b},^a and Quing Zhu^{1b},^{a,c,*}

^aWashington University in St. Louis, Optical and Ultrasound Imaging Lab,
Department of Biomedical Engineering, St. Louis, Missouri, United States

^bWashington University in St. Louis, Optical and Ultrasound Imaging Lab,
Department of Electrical and Systems Engineering, St. Louis, Missouri, United States

^cWashington University School of Medicine, Department of Radiology,
St. Louis, Missouri, United States

Abstract

Significance: “Difference imaging,” which reconstructs target optical properties using measurements with and without target information, is often used in diffuse optical tomography (DOT) *in vivo* imaging. However, taking additional reference measurements is time consuming, and mismatches between the target medium and the reference medium can cause inaccurate reconstruction.

Aim: We aim to streamline the data acquisition and mitigate the mismatch problems in DOT difference imaging using a deep learning-based approach to generate data from target measurements only.

Approach: We train an artificial neural network to output data for difference imaging from target measurements only. The model is trained and validated on simulation data and tested with simulations, phantom experiments, and clinical data from 56 patients with breast lesions.

Results: The proposed method has comparable performance to the traditional approach using measurements without mismatch between the target side and the reference side, and it outperforms the traditional approach using measurements when there is a mismatch. It also improves the target-to-artifact ratio and lesion localization in patient data.

Conclusions: The proposed method can simplify the data acquisition procedure, mitigate mismatch problems, and improve reconstructed image quality in DOT difference imaging.

© The Authors. Published by SPIE under a Creative Commons Attribution 4.0 International License. Distribution or reproduction of this work in whole or in part requires full attribution of the original publication, including its DOI. [DOI: [10.1117/1.JBO.27.8.086003](https://doi.org/10.1117/1.JBO.27.8.086003)]

Keywords: artificial neural network; breast cancer; deep learning; diffuse optical tomography.

Paper 220081GRR received Apr. 16, 2022; accepted for publication Aug. 3, 2022; published online Aug. 25, 2022.

1 Introduction

Near-infrared diffuse optical tomography (DOT) has shown success in breast cancer diagnosis and treatment response monitoring.¹⁻⁶ To reduce the ill-posed nature of the DOT inverse problem, prior information from other imaging modalities, such as magnetic resonance imaging (MRI),^{2,7} x-ray CT or mammography,^{8,9} and ultrasound (US),¹⁰⁻¹⁶ has been employed to improve DOT reconstruction accuracy.

Absolute imaging in DOT uses a single set of measurements to reconstruct spatially distributed absorption and scattering coefficients. However, absolute imaging is sensitive to mismatches between the experimental data and the forward model for several reasons, such as inaccurately known object geometry or uncertain optode coupling coefficients.¹⁷ Thus, “difference imaging,” which reconstructs target optical properties using measurements with and

*Address all correspondence to Quing Zhu, zhu.q@wustl.edu

without the target, is often used in DOT *in-vivo* imaging. Difference imaging can partially cancel out modeling errors that are invariant between the measurements. Typically, the image reconstruction is carried out using the difference between the measurements and a linearized approximation of the forward model.^{9,18,19} For example, in clinical breast patient studies, our group normalized the measured diffuse reflectance from the lesion side breast to the contralateral normal breast (the reference side) to produce a “perturbation” for imaging reconstruction.²⁰ In practice, a sequence of reference measurements is acquired, and then, according to the chest wall shown in the coregistered US images and the perturbation, the best reference is manually selected for reconstruction. These procedures can significantly increase the data acquisition and postprocessing time. On the other hand, the assumption made in difference imaging that the background properties of the lesion side and reference side are the same may be inaccurate in some cases in clinical studies, and such mismatch can cause incorrect estimation of the lesion’s optical properties and produce image artifacts.^{21–23}

Here, to simplify the data acquisition procedure and to avoid mismatch problems in DOT difference imaging, we propose a new approach using a deep artificial neural network (ANN) to generate perturbation from target measurements only. The ANN model is trained and validated on simulation data, including data generated with the realistic VICTRE breast phantom²⁴ and VICTRE breastMass software.²⁵ The performance of the model is then tested with simulations, phantom experiments, and patient data.

2 Methods

2.1 DOT System

A frequency-domain US-guided DOT method and system were used for simulations, phantom experiments, and patient data. The system was previously described in Ref. 26. Briefly, the light source consists of four laser diodes (with wavelengths of 730, 785, 808, and 830 nm) modulated at 140 MHz. The detection of diffuse reflectance is achieved by 14 parallel photomultiplier tube detectors. A local oscillator at 140.02 MHz is used to demodulate the detected signals to 20 kHz. Then the signals are digitized and sampled by two eight-channel A/D data acquisition cards. A US transducer in the middle of the DOT probe provides the coregistered B-scan US images.

2.2 Dataset

2.2.1 Simulation

A total of 43,398 sets of measurements from finite element method (FEM) and Monte Carlo simulations²⁷ were used: 80% were randomly chosen as the training set and the rest were used as the validation set. The training set was used to fit the model, and the validation set was used to determine the ANN structure and to select proper hyperparameters. Different target sizes, depths, shapes, and absorption and reduced scattering coefficients (μ_a and μ_s' , respectively) were considered. Tissue heterogeneity was simulated with realistic digital breasts.²⁴ The target and background properties of the training and validation dataset are given in Table 1. More details about the setup of the simulations can be found in Refs. 28 and 29.

To demonstrate the generalization of the model, we generated 180 additional sets of simulation data for testing. This dataset covered various target sizes, depths, and absorption coefficients, and we made sure that the μ_a and μ_s' of targets, the breast tissue, and the chest wall in this dataset were different from that of the training and validation sets.

2.2.2 Phantom experiments

To further evaluate the performance of the model, phantom experiments and patient data were used as the test set because they are more representative of future unseen clinical data. Two sets of solid targets with high contrast ($\mu_a = 0.23 \text{ cm}^{-1}$) and low contrast ($\mu_a = 0.11 \text{ cm}^{-1}$) were placed in Intralipid[®] solution with a μ_a of 0.015 cm^{-1} and a μ_s' of 7.3 cm^{-1} , both measured

Table 1 Target, tissue, and chest wall properties in the training and validation set.

	FEM	Monte Carlo
Target shape	Spherical	Spherical, irregular ²⁵
Target radius (cm) ^a	0.5 to 1.5	0.375 to 1.5
Target center depth (cm)	0.6 to 2.5	0.7 to 2.7
Target μ_a (cm ⁻¹)	0.08 to 0.30	0.10 to 0.30
Target μ_s' (cm ⁻¹)	4 to 8	7
Tissue μ_a (cm ⁻¹)	0.01 to 0.06	Digital breasts with 20% to 80% fat, ²⁴ no chest wall
Tissue μ_s' (cm ⁻¹)	4 to 8	
Chest wall depth (cm)	1.6 to 5	
Chest wall tilting angle (deg)	-10 to 10	
Chest wall μ_a (cm ⁻¹)	0.1 to 0.2	
Chest wall μ_s' (cm ⁻¹)	4 to 8	

^aFor nonspherical targets, the radii are calculated as half of the largest dimensions in the z direction.

at 730 nm.²⁶ These targets had diameters of 1, 2, and 3 cm and were placed at different depths (central depths of 1.5, 2, and 2.5 cm).

To demonstrate the advantage of the proposed method in avoiding reconstruction inaccuracy due to mismatch between the target and reference measurements, we also conducted phantom experiments with chest wall mismatch. A gelatin-intralipid phantom³⁰ with a μ_a of 0.076 cm⁻¹ and a μ_s' of 9.8 cm⁻¹ measured at 730 nm was used to simulate the chest wall. Chest wall mismatch was created by placing the chest wall deeper at the target side than the reference side.

2.2.3 Clinical data

Patient data from 43 benign (22 fibroadenomas or proliferative lesions (PL) and 21 low-risk benign lesions of fibrocystic changes or complex cysts) and 13 malignant cases were used to evaluate the performance of the proposed method. This group of 56 patients had an average age of 49.2 years (± 13.8 years). The lesion radii in the z-direction ranged from 0.5 to 1.5 cm. The study was approved by the local IRB and was HIPAA compliant. Written informed consent was obtained from all patients. The data used in this paper were deidentified.

2.3 Artificial Neural Network

In traditional difference imaging for US-guided DOT, the normalized perturbation, $pert$, was calculated from the frequency-domain measurements of the lesion-side breast normalized to the contralateral reference-side breast:

$$pert = \frac{U_l - U_r}{U_r} = \left(\frac{A_l}{A_r} \cos(\phi_l - \phi_r) - 1 \right) + j \frac{A_l}{A_r} \sin(\phi_l - \phi_r), \quad (1)$$

where U_l and U_r are the lesion-side and the reference-side measurements, respectively. Under the assumption that the only difference between the lesion side and the reference side is that the lesion has a higher absorption coefficient than the background, A_l should be smaller than A_r . Simulations have shown that the phase difference between the two sides $|\phi_l - \phi_r|$ does exceed 90 deg,³¹ thus the real part of the normalized perturbation should be between -1 and 0.

Multilayer perceptron (MLP), a type of feedforward ANN, can approximate any continuous mapping function from one finite-dimensional space to another,³² and this mapping function can

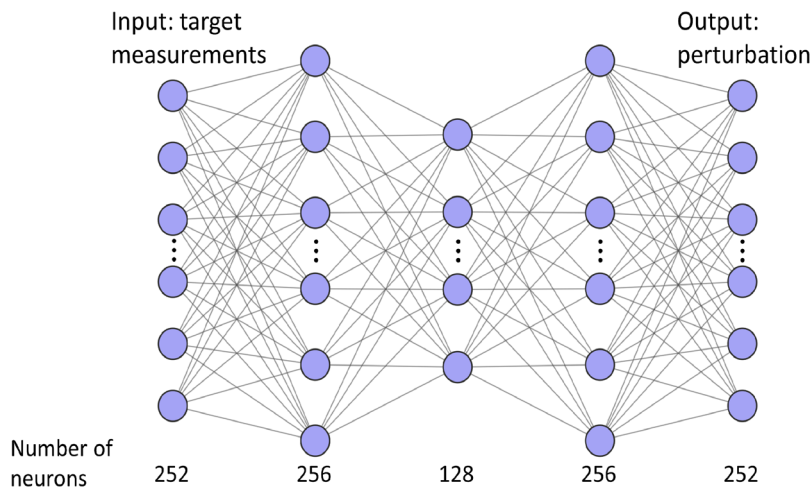


Fig. 1 ANN structure.

be learned using a data-driven approach. Hence, we trained an MLP-based ANN to output perturbation measurements $pert$ from target measurements U_l only. The nonlinear U_l -to- $pert$ mapping function, or the weight of the ANN, was learned from simulations with known U_l and $pert$.

As shown in Fig. 1, the input and output layers of the ANN both have 252 neurons, and the three hidden layers have 256, 128, and 256 neurons, respectively. To introduce nonlinearity to the neural network, a rectified linear unit activation function was used after each fully connected layer except the last one. The inputs of the network are the lesion side log amplitude, $\log(A_l \rho^2)$, and phase, ϕ_r , of simulated light reflectance on the lesion side with 2% random Gaussian noise added. Here, A_l is the amplitude and ρ is the source–detector distance. The outputs are the real and imaginary parts of the normalized perturbation. To avoid scaling problems for different datasets, the $\log(A_l \rho^2)$ values were variously offset in each set of measurements to keep the maximums of $\log(A_l \rho^2)$ the same. Similarly, the minimums of ϕ_r were kept the same. The output of the ANN is the real and imaginary parts of the normalized perturbation. The mean square error was used as the loss function. The network was implemented in PyTorch³³ and was trained for 200 epochs with a batch size of 64, using the Adam solver³⁴ with a learning rate of 1e-4 and a weight decay of 1e-5. Validation loss was monitored to avoid overfitting. The learning rate was reduced by a factor of 0.2 of its previous value when the validation loss did not decrease for three epochs. The training procedure took ~ 20 min on an NVIDIA Quadro P2000, and the testing procedure took < 0.1 s to generate a perturbation from one set of target measurements.

2.4 Image Reconstruction and Quantification

The DOT inverse problem was linearized using the Born approximation and was formulated as the following regularized optimization problem:³⁵

$$f(x) = \arg \min_{\delta\mu_a} \left(\|pert - W\delta\mu_a\|^2 + \frac{\lambda}{2} \|\delta\mu_a\|^2 \right). \quad (2)$$

Here, $\delta\mu_a$ represents the unknown changes in target μ_a compared with the reference side, W is a sensitivity matrix calculated using the Born approximation, and λ is a regularization parameter. The conjugate gradient algorithm and a dual mesh scheme using coregistered US guidance were employed to solve the inverse problem.³⁶ For patient data, the total hemoglobin (tHb) distribution was calculated using the reconstructed absorption maps of all four wavelengths.

For phantom data, the structural similarity index (SSIM) was used to evaluate the similarity between the reconstructed images and the ground truths. To evaluate the reconstructed image quality of patient data that did not have ground truths, we used a semiautomated CNN to segment lesions from the coregistered US images of the patient data.^{37,38} After each lesion was segmented, its x - and z -centroids were calculated (assuming the y -centroid to be 0), and the distance

between the centroid and the reconstructed lesion center of mass was calculated. For each depth in the reconstructed image, we defined the lesion area to be three times the US-segmented width from the x/y -centroid, defined outside to be the artifact area, and then we calculated $\max(\text{tHb}_{\text{target}}) / \max(\text{tHb}_{\text{artifact}})$.

The Wilcoxon rank sum test was used to evaluate the statistical significance, with a p -value of <0.05 being considered statistically significant. All image reconstruction and statistical tests were conducted using MATLAB 2021a.

3 Results

3.1 Testing on Simulation Data

For the 180 sets of simulation data in the test set, the averaged absolute difference between the reconstructed maximum μ_a from ANN predicted perturbation and from matched perturbation was 0.0068 cm^{-1} (95% CI: 0.0062 to 0.0074 cm^{-1}). Figure 2 shows one ground truth, simulated perturbation without mismatch, simulated perturbation with chest wall mismatch, ANN-predicted perturbation, and their corresponding reconstructed images. When there is no mismatch, the real part of the measured perturbation is negative and localized. When the reference side chest wall is shallower than the target side chest wall, both the real and imaginary parts of the perturbation move in the positive direction, and the target is not reconstructed. The ANN-predicted perturbation is similar to the perturbation without mismatch, and its corresponding reconstructed image shows a similar target shape, depth profile, and μ_a to the image using perturbation without mismatch.

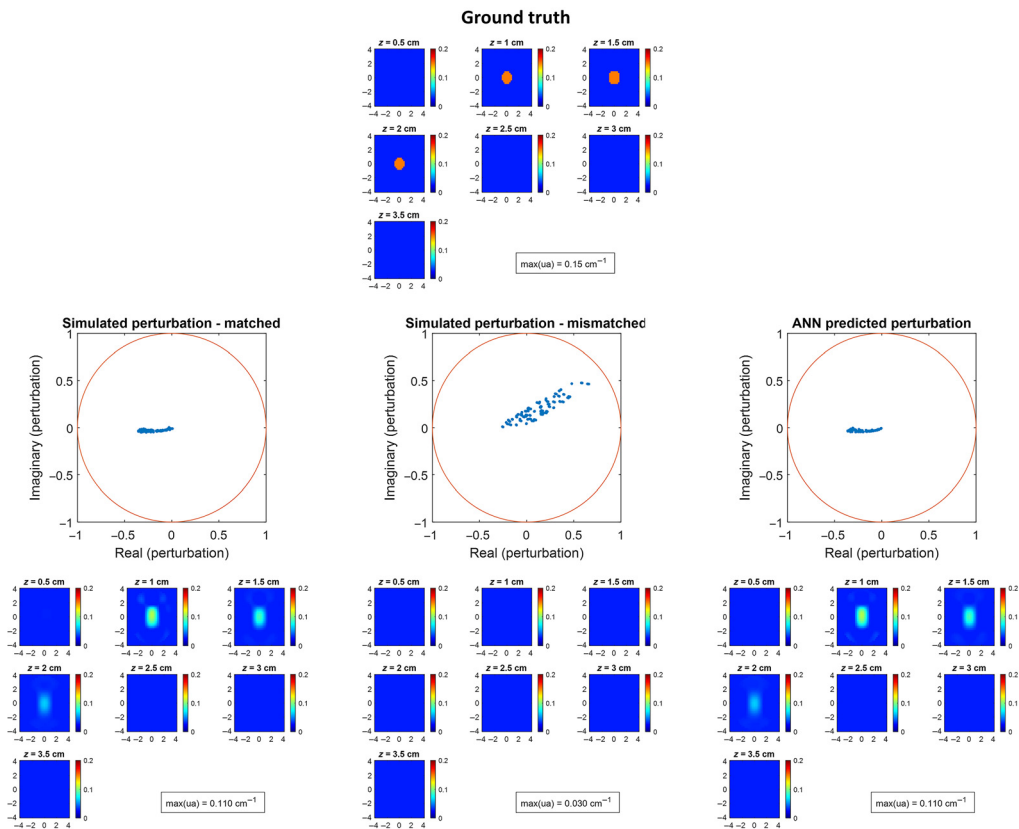


Fig. 2 Ground truth, simulated perturbation without chest wall mismatch (middle row, left), simulated perturbation with chest wall mismatch (middle row, middle), ANN-predicted perturbation (middle row, right), and their corresponding reconstructed images (bottom row). The target has $\mu_a = 0.15 \text{ cm}^{-1}$, radius = 1 cm, and depth = 1.5 cm. Chest wall depth is 3 cm on the target side and the matched reference side and is 2 cm on the mismatched reference side.

3.2 Testing on Phantom Data

Figure 3 shows images of phantoms reconstructed using the ANN-predicted perturbation and the measured perturbation. For high contrast targets, the two methods give similar reconstructed target sizes, shapes, and μ_a values. However, for low contrast targets, the reconstruction using the measured perturbation has distorted shapes, and the reconstructed μ_a values are lower than the ground truths, whereas the reconstruction using the ANN-predicted perturbation gives shapes and μ_a closer to the ground truths.

Figure 4 shows the maximum reconstructed μ_a for high and low contrast targets with different radii and depths. In all tested cases, except for the high contrast target with a 0.5-cm radius and a 1.5-cm depth, the ANN-predicted perturbations give the maximum reconstructed μ_a values closer to the ground truth than the measured perturbation does.

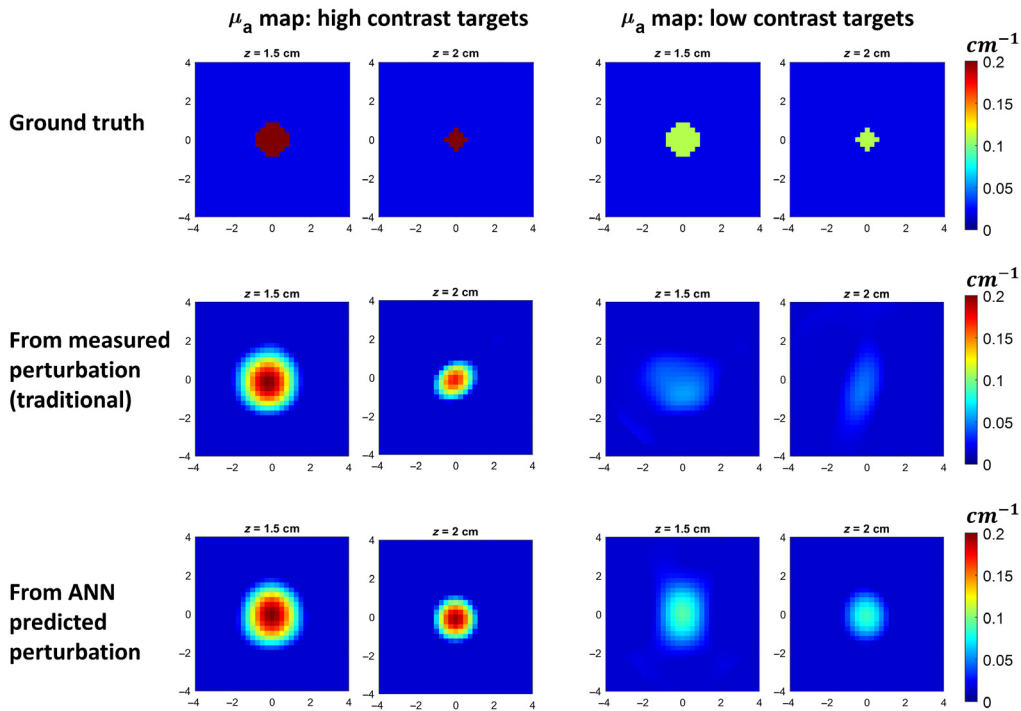


Fig. 3 Reconstructed phantom images of high and low contrast targets with different radii at a 2-cm depth. For better visualization, we show only the top layer of the reconstructed image containing the target.

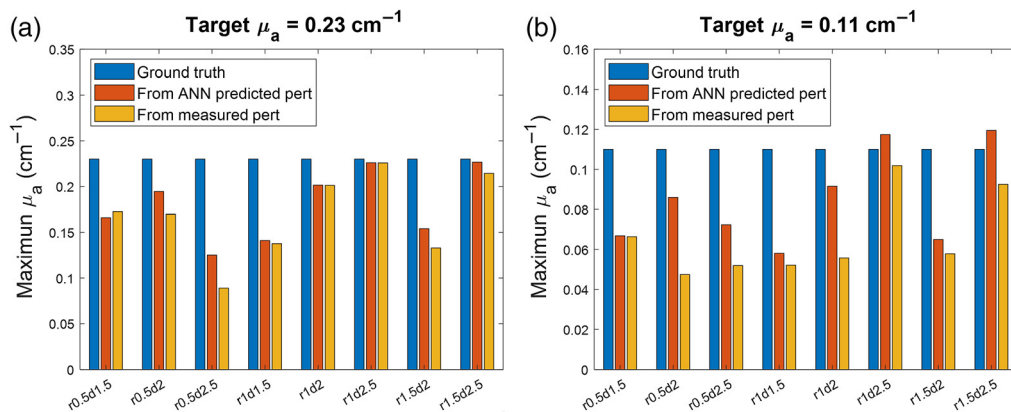


Fig. 4 The maximum reconstructed μ_a for (a) high and (b) low contrast targets with different radii (r) and depths (d).

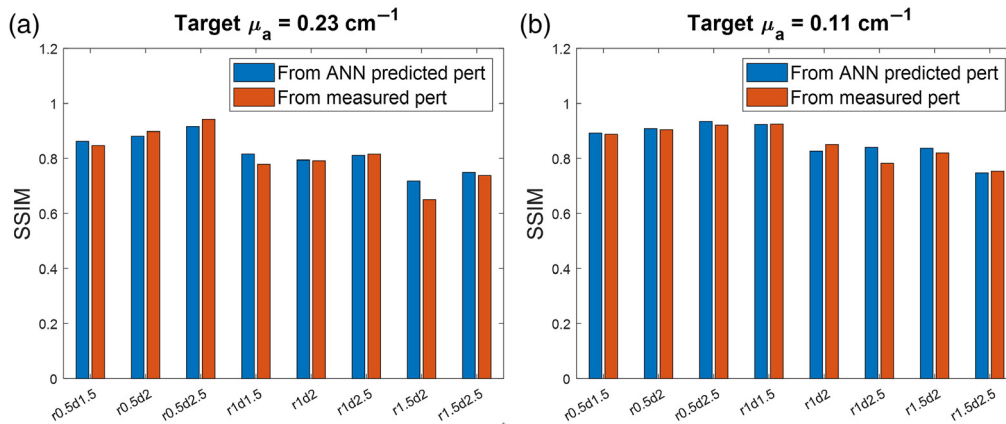


Fig. 5 SSIM values between reconstructed images and the ground truths for (a) high and (b) low contrast targets with different radii (r) and depths (d).

Figure 5 shows the SSIM values between the reconstructed images using the corresponding ground truths. For all tested cases, images generated using ANN-predicted perturbations have SSIM values higher than or similar to (difference $< 3\%$) those using measured perturbations.

Figure 6 shows measured perturbations without and with chest wall mismatch and the ANN-predicted perturbation and their corresponding reconstructed images. When there is no chest wall mismatch, the real part of the measured perturbation is negative and localized, with a few outliers. The reconstructed target is mostly located in the bottom layer. When the reference side chest wall is shallower than the target side chest wall, both the real and imaginary parts of the measured perturbation move in the positive direction, and the target is not reconstructed. The ANN-predicted perturbation generated an image that shows the target with three layers, which is closer to the ground truth than the other two.

3.3 Testing on Patient Data

Figure 7 shows representative tHb maps from three patients: one with a malignant tumor [Fig. 7(a)] and two with benign lesions [Figs. 7(b) and 7(c)]. To calculate the measured perturbation, the best reference was manually selected according to the chest wall position in the coregistered US image and the perturbation. Figure 7(a) shows the coregistered US image of a 59-year-old patient with invasive ductal carcinoma with a 1.1-cm deep lesion that measures 2.4 and 1.0 cm in the x - and z -directions, respectively. Figure 7(b) shows a 52-year-old patient with a benign cyst that is located 1.5 cm deep and measures 2.8 and 2.0 cm in the x and z directions, respectively. In Figs. 7(a) and 7(b), no significant mismatch was found by evaluating the coregistered US images and the measured perturbations. Compared with the measured perturbation, the ANN-predicted perturbation generated images with similar depth profiles and the maximum absorption coefficients, but they are more focused and centralized. Figure 7(c) shows a 48-year-old patient with a small pseudoangiomatous stromal hyperplasia that measures 1.4 and 0.8 cm in the x and z directions, respectively. By evaluating the measured perturbation, we found that there was a mismatch between the lesion and reference side measurements. In the reconstructed image, the lesion was not properly reconstructed and did not show up. Using the proposed deep learning-based approach, the lesion was successfully reconstructed in the corresponding area of the US image, using the perturbation generated from the target side measurements only. Figures 8(a) and 8(b) show box plots of the ratio of the maximum values of the reconstructed target tHb to the artifact tHb and the reconstructed center of mass to US segmented centroid distances for all 56 cases, respectively. The images reconstructed using the ANN-predicted perturbations have higher target tHb/artifact tHb ratios, and the lesions are closer to the US-segmented lesion positions.

Figure 9 shows box plots of the maximum tHb for 21 low-risk benign lesions, 22 fibroadenomas (fibro) or PL, and 13 malignant cases, reconstructed using the measured and ANN-predicted perturbations. The tHb values calculated for all target files were averaged for each

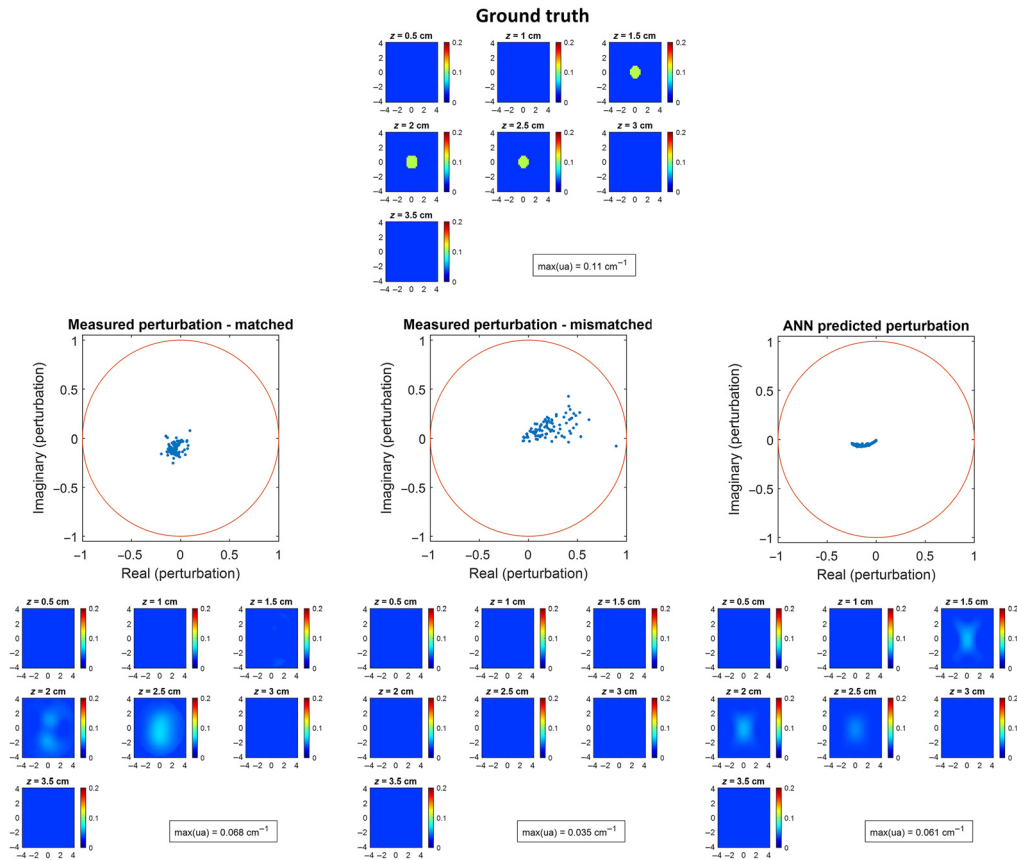


Fig. 6 Ground truth for phantom experiment with chest wall (top row), measured perturbation without chest wall mismatch (middle row, left), measured perturbation with chest wall mismatch (middle row, middle), ANN-predicted perturbation (middle row, right), and their corresponding reconstructed images (bottom row). The target has $\mu_a = 0.11 \text{ cm}^{-1}$, radius = 1 cm, and depth = 2 cm. Chest wall depth is 3 cm on the target side and the matched reference side and is 2 cm on the mismatched reference side.

patient. The tHb values reconstructed using the ANN-predicted perturbations are overall lower than those using the measured perturbations. The tHb maps of low-risk benign and malignant lesions reconstructed from the ANN-predicted perturbations are significantly different, although the p -value is slightly higher than those reconstructed from the measured perturbations calculated using the best manually selected references. For reconstructions using ANN-predicted perturbations, the PL/fibro group has larger variations than the other two groups.

4 Discussion

We designed an ANN to generate data for DOT difference imaging from target measurements only. The ANN was trained and validated using simulation data that included a wide range of realistic background tissues as well as target sizes, shapes, depths, and optical properties to account for individual differences in patients. To simulate the noise in actual measurements, we included Monte Carlo simulations that contain photon noise and added Gaussian noise to the simulated target measurements. The model was then tested with phantom and clinical data. It performed comparably to the approach using measurements without mismatch, and it outperformed the approach using measurements when there was a mismatch between the target and reference measurements. This is because the ground truths for training the ANN are the perturbations calculated from matched target and reference measurements. Hence, unlike the traditional approach in which the perturbation highly depends on the reference measurements, the ANN will always output a matched perturbation. This predictive approach can simplify data

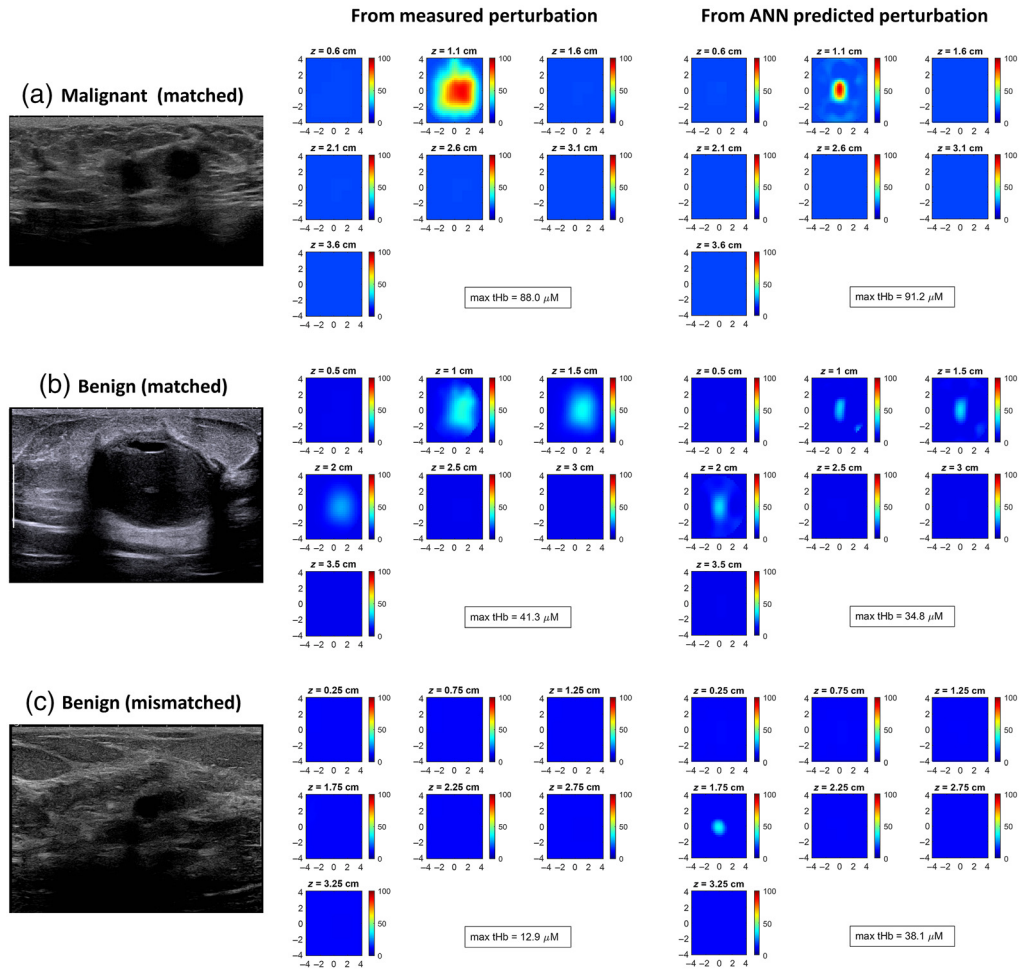


Fig. 7 Coregistered US images (left column), tHb maps reconstructed using the measured perturbation (middle column), and tHb maps reconstructed using the ANN-predicted perturbation (right column) for (a) a malignant tumor and (b) and (c) benign lesions. In (c), there is a mismatch between the lesion and reference side measurements. Color bars indicate the tHb level, in units of μM .

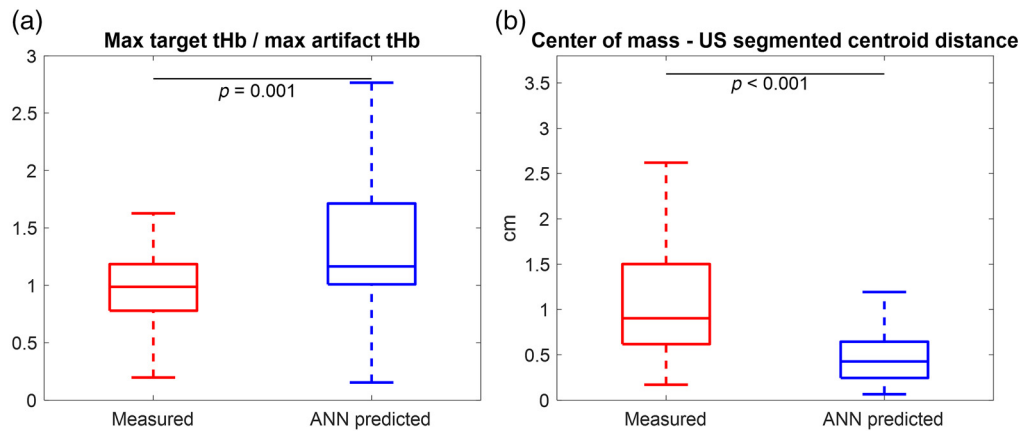


Fig. 8 Box plots of (a) the ratio of the maximum values of reconstructed target tHb over artifact tHb and (b) the reconstructed center of mass to US segmented centroid distance for all 56 lesions, using the measured and ANN-predicted perturbations.

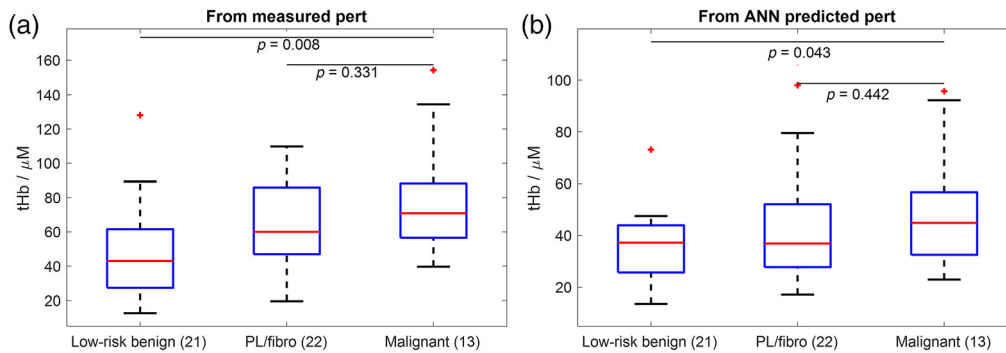


Fig. 9 Box plots of the maximum reconstructed tHb for 21 low-risk benign lesions, 22 fibroadenomas (fibro) or PL, and 13 malignant cases, using (a) measured perturbations and (b) ANN-predicted perturbations.

acquisition and mitigate mismatch problems in DOT difference imaging. It also improved the image quality in terms of the target-to-artifact-ratio and lesion localization.

This study has several limitations. First, the simulations included in the training set are limited. The proposed approach can be further improved using more complex simulations, such as larger lesions with peripheral Hb distribution, off-center lesions, and complex chest walls. Also, because perturbations without system noise were not available, we do not have ground truths for the phantom experiments, so we cannot fine-tune the ANN model with phantom experiments. However, when testing the trained model on phantom data, most of the images reconstructed using ANN-predicted perturbations were closer to the ground truth than those using true measurements without mismatch, indicating a good generalization of the model on experimental data. For patient data, the tHb values reconstructed using ANN-predicted perturbation are overall lower than those using measured perturbation; thus, a new and lower threshold for separating benign from malignant lesions must be set. The performance of the ANN is better than or comparable to that of the measured perturbation, regardless of target sizes, for phantom data (Figs. 4 and 5). Nevertheless, in clinical data, we found that the ANN performs better than the measurements in distinguishing smaller benign and malignant lesions with z dimensions ≤ 1 cm but worse in distinguishing larger lesions. This relatively poor performance likely reflects the fact that larger lesion produced perturbations are more difficult to completely separate from the tissue background. In addition, the ANN performance for 808 and 830 nm is worse than 730 and 785 nm, which may be related to the sensitivity of these two wavelengths to the chest wall. For a prospective clinical application, we would streamline the reconstruction based on lesion size measured by US and decide if the ANN model or measured perturbation would be used for reconstruction. Finally, for other DOT systems with different configurations, the ANN may be modified according to the specific DOT systems and retrained with the new data.

Disclosures

The authors declare that there are no conflicts of interest related to this article.

Acknowledgments

The authors acknowledge the funding support from U.S. National Cancer Institute (R01CA228047). We thank James Ballard for reviewing and editing the manuscript.

Code, Data, and Materials Availability

The associated code has been uploaded to Code Ocean, <https://codeocean.com/capsule/1476758/tree>. Data are available from the corresponding author upon reasonable request.

References

1. B. J. Tromberg et al., "Diffuse optics in breast cancer: detecting tumors in pre-menopausal women and monitoring neoadjuvant chemotherapy," *Imaging Breast Cancer* **7**, 279–285 (2005).
2. R. Choe et al., "Diffuse optical tomography of breast cancer during neoadjuvant chemotherapy: a case study with comparison to MRI," *Med. Phys.* **32**(4), 1128–1139 (2005).
3. E. Heffer et al., "Near-infrared imaging of the human breast: complementing hemoglobin concentration maps with oxygenation images," *J. Biomed. Opt.* **9**(6), 1152–1160 (2004).
4. Q. Zhu and S. Poplack, "A review of optical breast imaging: multi-modality systems for breast cancer diagnosis," *Eur. J. Radiol.* **129**(January), 109067 (2020).
5. B. Chance et al., "Breast cancer detection based on incremental biochemical and physiological properties of breast cancers: a six-year, two-site study," *Acad. Radiol.* **12**(8), 925–933 (2005).
6. D. R. Leff et al., "Diffuse optical imaging of the healthy and diseased breast: a systematic review," *Breast Cancer Res. Treat.* **108**(1), 9–22 (2008).
7. B. Brooksby et al., "Magnetic resonance-guided near-infrared tomography of the breast," *Rev. Sci. Instrum.* **75**(12), 5262–5270 (2004).
8. Q. Fang et al., "Combined optical imaging and mammography of the healthy breast: optical contrast derived from breast structure and compression," *IEEE Trans. Med. Imaging* **28**(1), 30–42 (2009).
9. Q. Zhang et al., "Coregistered tomographic x-ray and optical breast imaging: initial results," *J. Biomed. Opt.* **10**(2), 024033 (2005).
10. L. Wang et al., "Noninvasive measurement of placental hemodynamics with ultrasound-guided FD-diffuse optical spectroscopy," in *Optical Tomography and Spectroscopy*, Optical Society of America, p. SW4D-5 (2020).
11. T. Ko et al., "Quantifying placental oxygenation using ultrasound-guided frequency-domain near-infrared spectroscopy (FD-NIRS)," *Am. J. Obstet. Gynecol.* **216**(1), S172 (2017).
12. L. Cortese et al., "LUCA device: a multi-wavelength time-resolved spectroscopy and diffuse correlation spectroscopy device with an integrated clinical ultrasound module/probe," in *Optical Tomography and Spectroscopy*, Optical Society of America, p. SW4D-7 (2020).
13. C. Lindner et al., "Diffuse optical characterization of the healthy human thyroid tissue and two pathological case studies," *PLoS One* **11**(1), e0147851 (2016).
14. Q. Zhu et al., "Benign versus malignant breast masses: optical differentiation with US-guided optical imaging reconstruction," *Radiology* **237**(1), 57–66 (2005).
15. Q. Zhu et al., "Assessment of functional differences in malignant and benign breast lesions and improvement of diagnostic accuracy by using US-guided diffuse optical tomography in conjunction with conventional US," *Radiology* **280**(2), 387–397 (2016).
16. M. Zhang et al., "Target depth-regularized reconstruction in diffuse optical tomography using ultrasound segmentation as prior information," *Biomed. Opt. Express* **11**(6), 3331–3345 (2020).
17. M. Mozumder et al., "Nonlinear approach to difference imaging in diffuse optical tomography," *J. Biomed. Opt.* **20**(10), 105001 (2015).
18. D. Boas, T. Gaudette, and S. Arridge, "Simultaneous imaging and optode calibration with diffuse optical tomography," *Opt. Express* **8**(5), 263–270 (2001).
19. Q. Zhu, N. Chen, and S. H. Kurtzman, "Imaging tumor angiogenesis by use of combined near-infrared diffusive light and ultrasound," *Opt. Lett.* **28**(5), 337–339 (2003).
20. Y. Ardeshirpour, M. Huang, and Q. Zhu, "An optical tomography method that accounts for a tilted chest-wall in breast imaging," *Proc. SPIE* **7174**, 71740U (2009).
21. J. Heiskala, P. Hiltunen, and I. Nissilä, "Significance of background optical properties, time-resolved information and optode arrangement in diffuse optical imaging of term neonates," *Phys. Med. Biol.* **54**(3), 535–554 (2009).
22. Y. Ardeshirpour, M. Huang, and Q. Zhu, "Effect of the chest wall on breast lesion reconstruction," *J. Biomed. Opt.* **14**(4), 044005 (2009).
23. S. Li et al., "Effect and correction of optode coupling errors in breast imaging using diffuse optical tomography," *Biomed. Opt. Express* **12**(2), 689–704 (2021).

24. A. Badano et al., "Evaluation of digital breast tomosynthesis as replacement of full-field digital mammography using an *in silico* imaging trial," *JAMA Netw. Open* **1**(7), e185474 (2018).
25. L. De Sisternes et al., "A computational model to generate simulated three-dimensional breast masses," *Med. Phys.* **42**(2), 1098–1118 (2015).
26. H. Vavadi et al., "Compact ultrasound-guided diffuse optical tomography system for breast cancer imaging," *J. Biomed. Opt.* **24**(2), 021203 (2019).
27. Q. Fang and D. A. Boas, "Monte Carlo simulation of photon migration in 3D turbid media accelerated by graphics processing units," *Opt. Express* **17**(22), 20178 (2009).
28. Y. Zou et al., "Machine learning model with physical constraints for diffuse optical tomography," *Biomed. Opt. Express* **12**(9), 5720–5735 (2021).
29. S. Li, M. Zhang, and Q. Zhu, "Ultrasound segmentation-guided edge artifact reduction in diffuse optical tomography using connected component analysis," *Biomed. Opt. Express* **12**(8), 5320–5336 (2021).
30. J. R. Cook, R. R. Bouchard, and S. Y. Emelianov, "Tissue-mimicking phantoms for photoacoustic and ultrasonic imaging," *Biomed. Opt. Express* **2**(11), 3193–3206 (2011).
31. H. Vavadi et al., "Automated data selection method for diffuse optical tomography to improve the robustness of breast cancer detection," *Biomed. Opt. Express* **7**(10), 4007–4020 (2016).
32. K. Hornik, M. Stinchcombe, and H. White, "Multilayer feedforward networks are universal approximators," *Neural Netw.* **2**(5), 359–366 (1989).
33. A. Paszke et al., "PyTorch: an imperative style, high-performance deep learning library," in *Adv. in Neural Inf. Process. Syst. (NeurIPS)*, Vol. 32 (2019).
34. D. P. Kingma and J. L. Ba, "Adam: a method for stochastic optimization," in *3rd Int. Conf. Learn. Represent. ICLR 2015 – Conf. Track Proc.*, pp. 1–15 (2015).
35. K. M. S. Uddin and Q. Zhu, "Reducing image artifact in diffuse optical tomography by iterative perturbation correction based on multiwavelength measurements," *J. Biomed. Opt.* **24**(5), 056005 (2019).
36. M. Huang and Q. Zhu, "Dual-mesh optical tomography reconstruction method with a depth correction that uses a priori ultrasound information," *Appl. Opt.* **43**(8), 1654–1662 (2004).
37. M. Zhang et al., "Shape based reconstruction using ultrasound segmentation as prior in ultrasound-guided diffuse optical tomography," in *Optical Tomography and Spectroscopy, Optical Society of America*, p. JTh2A.4 (2020).
38. K. K. Maninis et al., "Deep extreme cut: from extreme points to object segmentation," in *Comput. Vis. and Pattern Recognit. (CVPR)*, pp. 616–625 (2018).

Shuying Li is a PhD candidate in the Department of Biomedical Engineering, Washington University in St. Louis. Prior to her PhD studies, she completed her bachelor's degree from Zhejiang University and her master's degree from the University of Michigan. She has been working on cancer diagnosis using optical imaging including diffuse optical tomography, optical coherence tomography, and spatial frequency domain imaging. She focuses on tackling practical problems in clinical/preclinical studies using algorithms and machine learning.

Menghao Zhang is a PhD candidate in the Department of Electrical and System Engineering, Washington University in St. Louis. He received his bachelor's degree from the University of Electronic Science and Technology of China in 2015. He is now working on ultrasound-guided diffuse optical tomography to improve breast cancer diagnosis.

Minghao Xue received his BS degree from Sun Yat-sen University, in China, in 2020, and started his doctoral studies in biomedical engineering at Washington University in Saint Louis in 2021. His research focuses on deep learning and ultrasound-guided diffuse optical tomography (US-guided DOT). Currently, he is working on the automated study of US-guided DOT clinical translation.

Quing Zhu joined Washington University in St. Louis in the Department of Biomedical Engineering in July 2016. Previously, she was a professor of electrical and computer engineering and biomedical engineering at the University of Connecticut. Her research interests are focused on multimodality photoacoustic, ultrasound, optical coherence tomography, and structured light imaging techniques for cancer detection and treatment assessment and prediction.